

Analysing one- and two-bit data to reduce memory requirements for \mathcal{F} -statistic-based gravitational wave searches

P. CLEARWATER,^{1,2} A. MELATOS,¹ S. NEPAL,² AND M. BAILES³

¹*OzGrav, University of Melbourne, Parkville, Victoria 3010, Australia*

²*Data61, Commonwealth Scientific and Industrial Research Organisation,
Corner Vimiera and Pembroke Roads, Marsfield, NSW 2122, Australia*

³*OzGrav, Swinburne University of Technology, Hawthorn, Victoria 3122, Australia*

ABSTRACT

Searches for continuous-wave gravitational radiation in data collected by modern long-baseline interferometers, such as the Laser Interferometer Gravitational-wave Observatory (LIGO), the Virgo interferometer and the Kamioka Gravitational Wave Detector (KAGRA), can be memory intensive. A digitisation scheme is described that reduces the 64-bit interferometer output to a one- or two-bit data stream while minimising distortion and achieving considerable reduction in storage and input/output cost. For the representative example of the coherent, maximum-likelihood matched filter known as the \mathcal{F} -statistic, it is found using Monte-Carlo simulations that the injected signal only needs to be ≈ 24 per cent stronger (for one-bit data) and ≈ 6.4 per cent stronger (for two bit data with optimal thresholds) than a 64-bit signal in order to be detected with 90 per cent probability in Gaussian noise. The foregoing percentages do not change significantly when the signal frequency decreases secularly, or when the noise statistics are not Gaussian, as verified with LIGO Science Run 6 data.

1. INTRODUCTION

A key class of targets for long-baseline gravitational-wave interferometers, such as the Advanced Laser Interferometer Gravitational-wave Observatory (aLIGO) (Aasi et al. 2015a), Virgo (Acernese et al. 2015) and the Kamioka Gravitational Wave Detector (KAGRA) (Akutsu et al. 2021), are persistent, quasi-monochromatic sources, called continuous-wave sources. An important class of continuous-wave emitters are neutron stars, which radiate at simple multiples of the stellar spin frequency f_* . Examples include the mass quadrupole radiation from quasistatic mountains (at f_* and $2f_*$) (Melatos & Payne 2005; Ushomirsky et al. 2000), current quadrupole radiation from r -modes (at approximately $4f_*/3$) (Bondarescu et al. 2009; Idrisy et al. 2015), or non-axisymmetric flows in superfluids with pinned vortices (at f_*) (Melatos et al. 2015). For a source of known spin frequency, a common search technique is to apply a coherent matched filter based on a maximum likelihood estimator called the \mathcal{F} -statistic (Jaranowski et al. 1998). If the spin frequency is unknown, semi-coherent search techniques are often preferred. In this paper we consider specifically the coherent \mathcal{F} -statistic, but semi-coherent techniques such as the hidden Markov model (Suvorova et al. 2016, 2017; Melatos et al. 2021), cross-correlation (Dhurandhar et al. 2008; Chung et al. 2011; Meadors et al. 2018), PowerFlux (Dergachev 2012, 2013), StackSlide (Brady & Creighton 2000; Pletsch & Allen 2009; Pletsch 2010; Wette 2015, 2016; Wette et al. 2018), TwoSpect (Goetz & Riles 2011; Meadors et al. 2016) and the Hough transform (Krishnan et al. 2004; Astone et al. 2014) may also benefit from the ideas presented.

One challenge faced by gravitational wave data analysis is the large volume of data involved. Typically, a continuous-wave search processes 30-minute short Fourier transforms (SFTs), sampled typically at kilohertz rates. Data in SFTs are normally stored using 64 bit values for each sample. Each SFT file consumes 14.4 kilobytes per 1 Hz of bandwidth. For a typical year-long run, this translates to approximately 250 gigabytes, per detector, to cover a 1 kHz band. While this is not a problem to store at present, a search that processes the whole dataset in a random-access manner [such as a cross-correlation-style search (Chung et al. 2011)] can be slowed drastically due to input/output (I/O) overhead when processing more data than can be stored in random access memory (RAM). Moreover, as search algorithms and data collection practices evolve, and new generations of interferometers are constructed, there may come a time in the future when memory limitations pose greater challenges than one envisions now, as occurred historically with the move to baseband recording in pulsar radio astronomy, e.g. Stairs et al. (2000).

In this paper, we show that \mathcal{F} -statistic-based searches work almost as well on one- and two-bit digitisations of the original 64-bit data. This approach has been exploited in other low-signal-to-noise searches for periodic signals in astronomy, such as radio pulsar timing and search experiments (Manchester et al. 1996; Jenet & Anderson 1998). The paper is structured as follows. In Section 2, we discuss and quantify the distortion introduced by digitisation. In Section 3, we review the \mathcal{F} -statistic and define the multiple digitisation schemes we investigate. In Section 4, we report the results of Monte-Carlo performance tests on the various digitisation schemes, with and without frequency evolution. In Section 5, we investigate how the results change, when the noise statistics are not Gaussian. In Section 6, we discuss briefly the path to implementing the technique in existing software libraries for gravitational wave data analysis.

2. OPTIMAL DIGITISATION

Storing an analogue signal as a digital file always involves a choice of how to encode the data. The standard choice for science data collected from gravitational wave interferometers is to store strain data in files called frame files, as Institution of Electrical and Electronics Engineers standard 754 (IEEE 2008) 64-bit double-precision floating point numbers (Blackburn et al. 2009). When these frame files are converted into SFTs, the SFT files store two single-precision (32-bit) floating point numbers for each frequency bin, corresponding to the real and imaginary components, giving an effective 64-bits of precision (Allen et al. 2022). The error introduced by digitisation to 64 bits is small compared to the error arising from filtering in the interferometer’s analogue-to-digital (ADC) converter, as long as the ADC output exceeds about 13 bits, which suggests that 64 bits per bin in the SFT files may be an unnecessary level of precision. For a detailed discussion of ADC digitisation noise, see Allen & Brady (1997).

It is a counter-intuitive fact that signal processing algorithms operating under low signal-to-noise conditions suffer remarkably little degradation in sensitivity when the data are truncated from 64 bits to (say) one or two bits. Qualitatively, this happens because one faces rapidly diminishing returns from greater precision: there is no point measuring detector output precisely if the signal is weak, because most of that effort goes into measuring the noise. The search for continuous gravitational waves from neutron stars is an example of such a low signal-to-noise case. Furthermore the signal-to-noise ratio stays low throughout the observation, because the signal has constant amplitude. (One may compare to radio pulsars, where focusing by the interstellar medium can temporarily magnify the signal-to-noise ratio, in which case digitisation costs sensitivity.) Digitisation can also improve the robustness of a search by filtering out short-duration glitches.

The general theory of waveform distortion and sensitivity loss through digitisation was laid out in detail by Max (1960) and subsequently applied to radio pulsar astronomy by Jenet & Anderson (1998). We summarise the main points in this section to provide a framework for the application that follows. We refer the reader to the aforementioned references for a fuller treatment of the subject.

Consider a continuous, real-valued time series $x(t)$. Suppose we construct a digitised version of $x(t)$, denoted by $\hat{x}(t)$, by mapping the N discrete intervals $[x_i, x_{i+1})$ ($i = 1, \dots, N$) to the N discrete values y_i . Specifically, we have $\hat{x}(t) = y_i$ for $x_i \leq x(t) < x_{i+1}$ at every sampled instant t . The first and last endpoints are necessarily $x_1 = -\infty$ and $x_{N+1} = +\infty$ to ensure the digitiser covers the full input range. The task is to minimise the distortion introduced by digitisation, which is equivalent to minimising the expected value

$$\rho^2 = \langle [x(t) - \hat{x}(t)]^2 \rangle, \quad (1)$$

where $x(t)$ is a random variable equal to the signal plus the noise¹. Equation (1) is minimised with respect to x_2, \dots, x_N , yielding the $N - 1$ simultaneous equations

$$x_i = (y_{i-1} + y_i)/2, \quad \text{for } i = 2, \dots, N, \quad (2)$$

and also minimised with respect to y_1, \dots, y_N , yielding the N simultaneous equations

$$0 = \int_{x_i}^{x_{i+1}} dx (x - y_i)p(x), \quad \text{for } i = 1, \dots, N, \quad (3)$$

where $p(x)$ is the probability density function of the sampled time series $x(t)$.

¹ The mean-square error in equation (1) is not the only valid measure of distortion of course, but it is favoured in the literature (Max 1960; Jenet & Anderson 1998).

In what follows, we solve Equations (2) and (3) for Gaussian noise with standard deviation σ in the low signal-to-noise regime, i.e., $p(x) \approx (2\pi\sigma)^{-1/2} \exp(-x^2/2\sigma^2)$. The results are given in Section 3. Strictly speaking, for gravitational wave applications, it is better to minimise the distortion of the \mathcal{F} -statistic itself, rather than the input time series, but the results reported in Section 3 are excellent in practice without this hard-to-calculate refinement, so we defer it to future work.

3. FEW-BIT \mathcal{F} -STATISTIC SEARCHES

3.1. \mathcal{F} -statistic

The \mathcal{F} -statistic (Jaranowski et al. 1998) is a maximum-likelihood estimator for the log likelihood of detecting a gravitational wave signal at a specific frequency (and its time derivatives) and sky position in noisy interferometer data. The \mathcal{F} -statistic accounts for modulation in the signal caused by the Earth’s rotation and its orbital motion about the Sun. An explicit recipe for calculating \mathcal{F} from the interferometer output (in the form of Fourier transforms), antenna pattern functions, noise spectral density, and phase model is given in Section 3 of Jaranowski et al. (1998) and is not reproduced here.

Given stationary, Gaussian noise with no signal, $2\mathcal{F}$ is distributed according to a chi-squared distribution with four degrees of freedom, whose probability density function (PDF) we denote by $\chi_4^2(\lambda = 0)$, where λ is the non-centrality parameter (zero when there is no signal). Given a desired false alarm probability α , the formula

$$\alpha = \int_{2\mathcal{F}_c}^{\infty} d(2\mathcal{F}) \chi_4^2(\lambda = 0; 2\mathcal{F}) \quad (4)$$

defines a detection threshold $2\mathcal{F}_c$.

In the presence of a signal, the \mathcal{F} -statistic is distributed according to a non-central χ^2 distribution (again with four degrees of freedom), where the non-centrality parameter λ depends on the dimensionless wave strain h_0 , the one-sided detector noise spectral density $S_h(f)$ at the observing frequency f , and the observation time T_{obs} according to

$$\lambda = \frac{Ah_0^2 T_{\text{obs}}}{S_h(f)}. \quad (5)$$

The constant of proportionality A depends on the various parameters describing the source and detector orientation. If some of those parameters are unknown, they can be averaged over (Jaranowski et al. 1998). Given a desired false dismissal probability β , the condition

$$\beta = \int_0^{2\mathcal{F}_c} d(2\mathcal{F}) \chi_4^2(\lambda; 2\mathcal{F}) \quad (6)$$

implicitly defines a squared signal-to-noise ratio λ corresponding to the threshold $2\mathcal{F}_c$.

If a search is done over N statistically independent measurements, the total false alarm probability is

$$\alpha_N = 1 - \left[\int_0^{2\mathcal{F}_c} d(2\mathcal{F}) \chi_4^2(\lambda = 0; 2\mathcal{F}) \right]^N. \quad (7)$$

In the tests performed in the next section, we search over a band spanning 1.06 Hz for an observing time of $T_{\text{obs}} = 48$ hours. The LIGO–Virgo–KAGRA Algorithms Library (LALSuite) (LIGO Scientific Collaboration et al. 2018) \mathcal{F} -statistic implementation, `lalpulsar_ComputeFStatistic_v2` (formerly known as `lalapps_ComputeFStatistic_v2`), takes the frequency spacing as a parameter that zero-pads the time series, which enables the user to select a frequency bin size. The frequency spacing is sometimes related colloquially to an over-resolution parameter, r , in the literature (Sammot et al. 2014), although it does not correspond necessarily to over-resolution in the strict sense. A typical choice (and incidentally the default value), which we follow here, is to space the bins by $1/(2T_{\text{obs}})$ (i.e. $r = 2$), used for example in many published continuous wave searches (Aasi et al. 2015b; Abbott et al. 2017b, 2019; Middleton et al. 2020; Millhouse et al. 2020; Beniwal et al. 2021; Abbott et al. 2022b,a). Hence, the number of \mathcal{F} -statistic frequency bins is $N_{\text{bins}} = 1.06 \text{ Hz} \times 172\,800 \text{ s} \times 2 = 366\,336$, and the frequency bin size is $1/(2T_{\text{obs}}) = 2.89 \times 10^{-6} \text{ Hz}$.

In passing we note that the assumption of statistical independence in the previous paragraph is often not true: when searching over a region of parameter space, search points that are close in parameter space have similar parameters, and

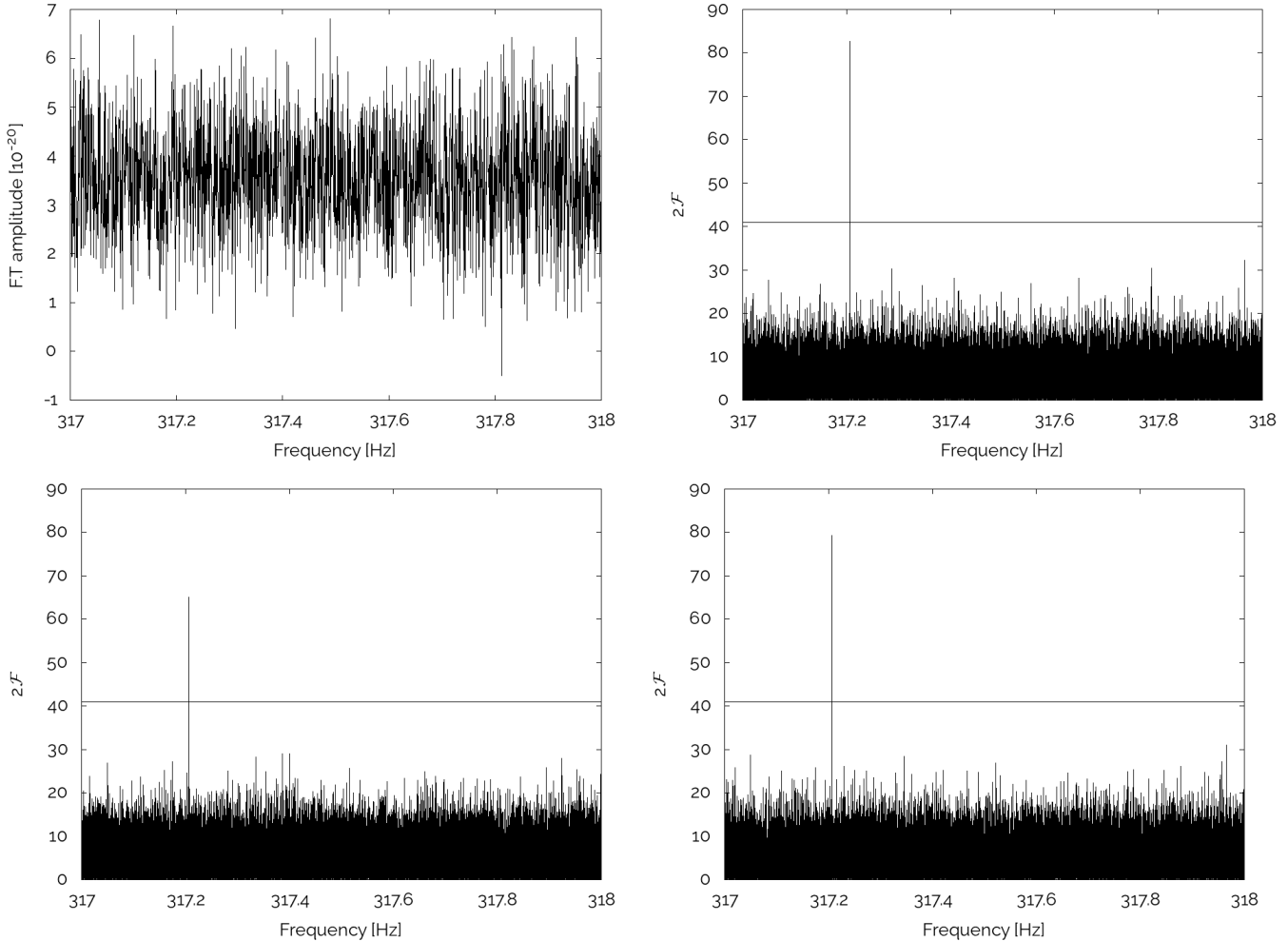


Figure 1. Representative plot of the search output from one noise realisation, including an injected signal with the parameters in Table 1 and a signal strength of $h_0 = 6 \times 10^{-25}$. The horizontal axis is the observing frequency. The top left plot displays the summed squared modulus of the 96 short Fourier transforms in the data set; no signal is visible. The top right plot displays the \mathcal{F} -statistic with full 64-bit digitisation; the signal is visible at 317.26 Hz. The bottom left and bottom right plots display the \mathcal{F} -statistic with one- and two-bit digitisation respectively. The horizontal bar is the critical threshold $2\mathcal{F}_c = 40.96$.

the \mathcal{F} -statistic is therefore correlated. Assuming instead that the \mathcal{F} -statistic is independent is conservative (causing the false alarm probability to be overstated) and so is favoured in the literature, although more scrutiny is being applied to the assumption recently (Tenorio et al. 2022). For this paper, we adopt the assumption of statistical independence. In the tests described below, we check the actual false alarm rate to ensure that it is at the level expected.

For the purposes of the tests described in the rest of this paper, we choose $\alpha_N = 0.01$ and $\beta = 0.1$. Solving Equations (6) and (7) with these probabilities yields $2\mathcal{F}_c = 40.96$. These choices of false alarm and false dismissal probability are typical for continuous gravitational wave searches (Abbott et al. 2005a,b), although we note that N varies widely amongst searches.

3.2. Digitisation scheme

We test the performance of the \mathcal{F} -statistic for several one- and two-bit digitisation schemes. Besides the optimal scheme described in Section 2, we examine some suboptimal but intuitively natural schemes to test whether or not the results are sensitive to how the digitisation intervals and output values are selected.

For one-bit digitisation, we simply apply the sign function to the input signal:

$$\hat{x}(t) = \begin{cases} +1, & \text{if } x(t) \geq 0, \\ -1, & \text{if } x(t) < 0. \end{cases} \quad (8)$$

The means of $x(t)$ and $\hat{x}(t)$ are zero, so Equation (8) does not introduce a DC bias. The \mathcal{F} -statistic value is independent of the total input power, so we do not need to normalise $\hat{x}(t)$.

For two-bit digitisation, we apply the four-level function

$$\hat{x}(t) = \begin{cases} -3, & x_1 \leq x(t) < x_2, \\ -1, & x_2 \leq x(t) < x_3, \\ +1, & x_3 \leq x(t) < x_4, \\ +3, & x_4 \leq x(t) < x_5. \end{cases} \quad (9)$$

Again, we do not normalise $\hat{x}(t)$. We do choose arbitrary output values that are equally spaced, a point to which we return below.

We test three approaches to choosing the thresholds x_1, \dots, x_5 . For a zero-mean signal in Gaussian noise, there is no loss of generality in choosing $x_1 = -\infty$, $x_3 = 0$ and $x_5 = +\infty$. As the PDF of $x(t)$ is symmetric, we also have $x_2 = -x_4$, leaving x_4 to be specified.

In the first approach, we set $x_4 = \max|x(t)|/2$, where the maximum is computed empirically from the whole measured time series. The drawback is that the maximum is usually a many-sigma outlier, so few samples are actually digitised to the ± 3 levels.

In the second approach, we seek to map equal numbers of samples to each output level. We set x_3 to equal the median sample to create two equal-size partitions and set x_2 and x_4 to the medians of the two partitions. This recipe does not guarantee $x_3 = 0$ and $x_2 = -x_4$ exactly, but in practice these relations hold to a good approximation for large data sets. Note that substantial pre-processing is needed to determine the quartiles.

A third approach follows the methodology developed in Max (1960), and summarised in Section 2, for choosing optimal thresholds. For a Gaussian distribution with standard deviation σ , equations (2) and (3) with $N = 4$ can be solved to yield $x_1 = -\infty$, $x_2 = -0.9816\sigma$, $x_3 = 0$, $x_4 = 0.9816\sigma$ and $x_5 = \infty$. The corresponding output levels are $y_1 = -1.510\sigma$, $y_2 = -0.4528\sigma$, $y_3 = 0.4528\sigma$, $y_4 = 1.510\sigma$. The optimal output levels are not equally spaced, as in equation (9), but they are within 15 per cent of being so. As the \mathcal{F} -statistic is independent of input power, σ may be chosen arbitrarily for our purposes in y_1, \dots, y_4 (but not in x_1, \dots, x_5 of course).

4. PERFORMANCE TESTS WITH GAUSSIAN NOISE

4.1. Monte-Carlo simulations

We compare the detection performance of the \mathcal{F} -statistic for one-, two-, and 64-bit digitisation by simulating multiple realisations of the gravitational wave signal from an isolated, triaxial rotator with spin frequency f_0 superposed on stationary Gaussian noise. The fixed source and noise parameters in each realisation are given in Table 1.

We inject signals with wave strains in the range $0.5 \times 10^{-25} \leq h_0 \leq 10.0 \times 10^{-25}$, in step sizes of 0.5×10^{-25} . The one-sided noise amplitude spectral density, $\sqrt{S_h(2f_0)} = 2 \times 10^{-23} \text{ Hz}^{-1/2}$, is chosen to be characteristic of the initial LIGO design. Hence the chosen h_0 values correspond to values of $h_0 [T_{\text{obs}}/S_h(2f_0)]^{1/2}$ between 1.0 and 20.8. For each digitisation scheme, 200 realisations are created for each h_0 value to measure the detection probability.

The synthetic noise and signals are generated using the LALSuite (LIGO Scientific Collaboration et al. 2018) tool `lalpulsar_Makefakedata_v4` (formerly known as `lalapps_Makefakedata_v4`). The tool produces either a time series or a sequence of SFTs. In this paper we run two kinds of tests. Sometimes we digitise the time series, whereupon we use `lalpulsar_Makefakedata_v4` to produce the time series, apply the desired digitisation scheme, create the SFTs by using FFTW (Frigo & Johnson 2005) and output them in the SFTv2 format (Allen et al. 2022). Sometimes we digitise the SFTs, whereupon we use `lalpulsar_Makefakedata_v4` to produce SFTs, and then separately digitise the real and imaginary values to produce new, digitised SFTs.

The resulting files are in the same format as standard SFTs, which means that they can be consumed directly by LALSuite tools. However, in order to realise the savings of digitisation, a new SFT in-memory format would have to be developed, with LALSuite tools modified to read and write to that format.

Table 1. Fixed source parameters for Monte-Carlo simulations.

Variable	Symbol	Value	Units
Reference GPS start time		875 936 746	s
Observation time	T_{obs}	172 800	s
Right ascension	α	0.092408204211	rad
Declination	δ	-0.956660382019	rad
Inclination angle	$\cos \iota$	-0.987561752324	
Polarisation angle	ψ	0.423734950335	rad
Initial phase	Φ_0	3.691030880249	rad
Spin frequency	f_0	317.207201716543	Hz
Noise amplitude spectral density	$\sqrt{S_h(2f_0)}$	2×10^{-23}	$\text{Hz}^{-1/2}$

The search is performed using the LALSuite tool `lalpulsar_ComputeFstatistic_v2` (Prix 2011), and is run with the search parameters (other than frequency) exactly matching the injection parameters, to ensure no loss in signal strength due to a mismatch between search and injection parameters. As explained above, we search a 1.06 Hz band containing the injected signal, thus searching over N_{bins} choices of frequency. By doing this search (rather than just calculating the \mathcal{F} -statistic for the injection bin), we mimic a real search which typically searches frequency over sub-bands ~ 1 Hz wide (Abbott et al. 2017b, 2019), and use the band to set a detection threshold through Equation (4). Of course, a real search may search over additional search parameters, or a narrower sub-band, if the frequency is measured electromagnetically with high accuracy: the choice to search over frequency in these tests is for illustration. We claim a detection if the bin containing the frequency of the injected signal returns $2\mathcal{F} > 40.96$, corresponding to a one per cent false alarm rate.

In claiming a detection, we consider the value of $2\mathcal{F}$ only in the bin containing the injection frequency and so disregard other bins, even those over the threshold $2\mathcal{F}_c$. An alternative approach would be to claim a detection when any bin in the search band exceeds the threshold, which of course is the only option available in an astrophysical search, when the signal frequency is often unknown. The principal aim of this paper is to compare different digitisation methods to full-precision processing, rather than to quantify the absolute sensitivity of a search, so for simplicity we take the approach of looking only in the injection bin. For the Monte Carlo simulations with Gaussian noise, we nevertheless monitor the whole search band for values that exceed $2\mathcal{F}_c$ (other than those forming part of the signal peak), to assure that the false alarm rate does not exceed $\alpha = 0.01$.

Weak sidelobes are observed in the \mathcal{F} -statistic output at $f_0 \pm 9 \times 10^{-6}$ Hz and $f_0 \pm 3.5 \times 10^{-5}$ Hz, whose origin is uncertain but likely due to the diurnal motion of the Earth, which is not completely accounted for by the \mathcal{F} -statistic due to approximations in its implementation (Prix 2007, 2011). They are not at the diurnal frequency $1/(86\,400\text{ s}) = 1.16 \times 10^{-5}$, or a multiple thereof, perhaps due to an interaction with the 1800 s SFT length. The sidelobes are not germane to what follows.

4.2. Detection probability

Figure 1 compares the output of the \mathcal{F} -statistic for one-, two- and 64-bit digitisation for one representative realisation with $h_0 = 6 \times 10^{-25}$ and f_0 as given in Table 1. The first panel shows the summed output (squared modulus) of the 96 SFTs for the full simulated observation. No signal is discernible at f_0 . The second panel shows the \mathcal{F} -statistic plotted versus frequency with full 64-bit digitisation. The signal is now clearly apparent as a spike at f_0 , with $2\mathcal{F} = 82.6$. The third and fourth panels show the \mathcal{F} -statistic output with one- and two-bit digitisation (optimal scheme, see Section 3.2). The results are remarkably similar to the second panel. The signal is clearly detected in both the one- and two-bit cases, with $2\mathcal{F} = 65.0$ and 79.3 respectively. In other words, digitisation causes a modest and tolerable loss of \mathcal{F} -statistic power.

Figure 2 compares two- and 64-bit digitisation for the three approaches to two-bit digitisation described in Section 3.2. It plots the fraction of realisations that yield a successful detection ($2\mathcal{F} > 2\mathcal{F}_c$) versus A^{-1} times the signal-to-noise ratio λ , i.e., $h_0[T_{\text{obs}}/S_h(2f_0)]^{1/2}$. Digitisation does not affect the overall shape of the curve. As expected, the 64-bit analysis leads to the highest detection probability. Two-bit digitisation reduces the detection probability modestly at all signal-to-noise ratios. Of the digitised curves, choosing $x_4 = \max|x(t)|/2$ leads to the poorest detection performance,

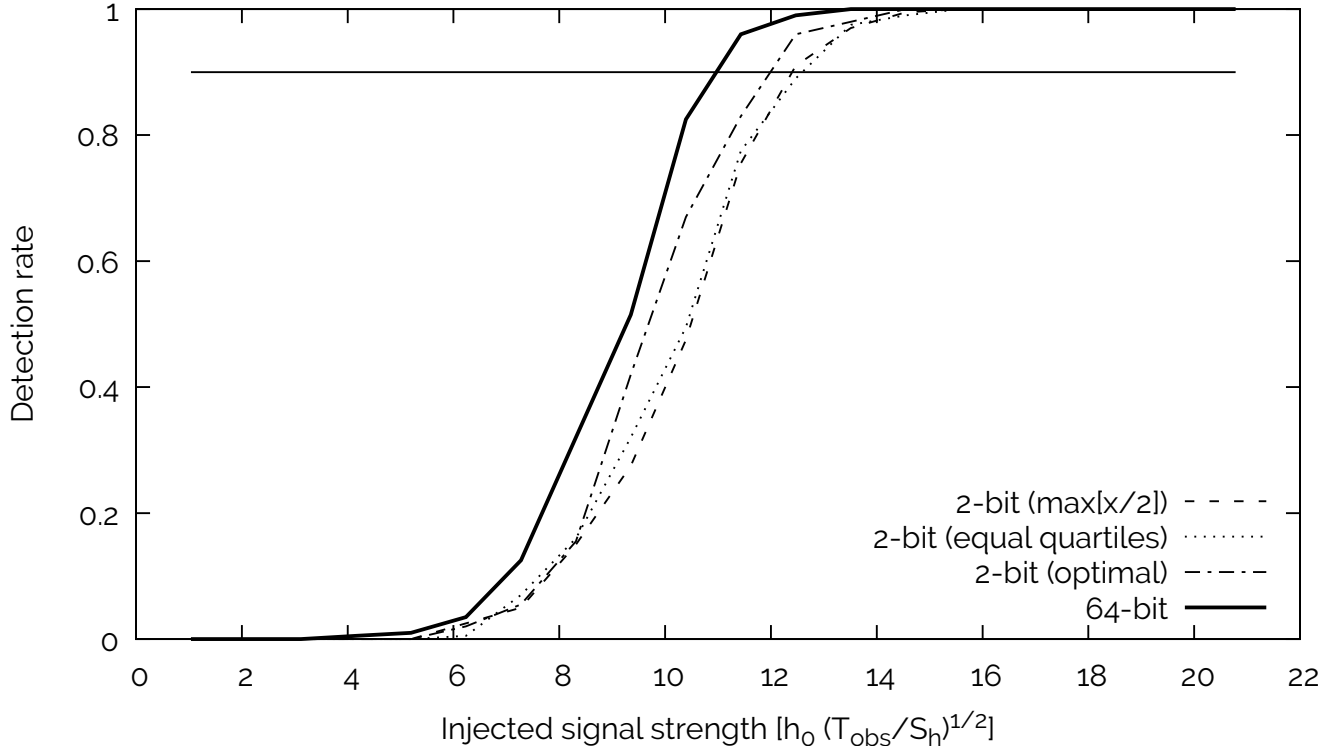


Figure 2. \mathcal{F} -statistic detection fraction versus injected signal-to-noise ratio $h_0[T_{\text{obs}}/S_h(f_0)]^{1/2}$ for 64-bit time series (control) and three choices of two-bit digitisation: using $\max|x(t)|/2$ as a threshold, using four equal-size quartiles, and using the optimal thresholds (see legend). The detection probability is computed from 200 realisations, with $2\mathcal{F}(f_0) > 40.96$ counting as a detection from Equation (7) with $\alpha_N = 0.01$. The horizontal line corresponds to 90 per cent detection probability, that is, a false dismissal probability of $\beta = 0.1$.

but even then the recovered \mathcal{F} -statistic value drops by just 11 per cent relative to a full 64-bit analysis. Equally weighted quartiles yield intermediate performance, and the optimal thresholds deliver, unsurprisingly, the best two-bit performance. The reduction in \mathcal{F} -statistic value for optimal thresholds is 6.4 per cent relative to a 64-bit analysis.

Figure 3 compares full 64-bit digitisation against one-bit digitisation of the time series and the SFT. When digitising the SFT, the resulting \mathcal{F} -statistic exhibits a different PDF from the expected chi-squared distribution, as discussed further in Section 4.3. We empirically determine that the critical threshold to achieve a false alarm probability of $\alpha_N = 0.01$ with one-bit digitised SFTs equals $2\mathcal{F}_c = 26.09$. As with two-bit digitisation, the shapes of all three curves are similar; essentially they are horizontally shifted relative to one another. Digitisation of the time series (24 per cent sensitivity loss) is marginally more effective than digitisation of the SFTs (29 per cent sensitivity loss).

The intersection between the horizontal line indicating a 90 per cent detection probability and each curve in Figures 2 and 3 indicates how much stronger a signal must be in order to be detected in few-bit digitised data. These values are summarised, for the representative case of $\alpha_N = 0.01$, $\beta = 0.9$ in Table 2 for the six digitisation schemes considered. While the sensitivity losses listed in Table 2 cannot be ignored, it is possible to recover full sensitivity by using a one- or two-bit digitised search as a first pass with a lower threshold (i.e. higher α_N) to identify likely signals. Those candidates can then be reprocessed using the full precision data.

4.3. PDF of \mathcal{F} -statistic applied to digitised data

For completeness, we present the empirical PDF of the \mathcal{F} -statistic after one-bit digitisation in Figure 4. We find that the PDF is unchanged to an excellent approximation, relative to double-precision processing, when the time series is digitised to one bit; the discrepancy is not discernible by eye.

When the SFTs are digitised, as opposed to the time series, the \mathcal{F} -statistic PDF does change (see histograms in bottom row) and exhibits a thinner tail than its 64-bit counterpart. The top left panel shows the \mathcal{F} -statistic PDF in

Table 2. Strength of an injected signal necessary to achieve 90 per cent detection efficiency at $\alpha_N = 0.01$, as a function of digitisation scheme. The efficiency is determined empirically from 10^3 Monte Carlo realisations.

Digitisation scheme	$h_0 \sqrt{T_{\text{obs}}/S_h}$
64-bit	11.08
2-bit, time series, optimal	11.79
2-bit, time series, $\max x(t) /2$	12.57
2-bit, time series, equal quartiles	12.58
1-bit, time series	13.78
1-bit, SFTs	14.30

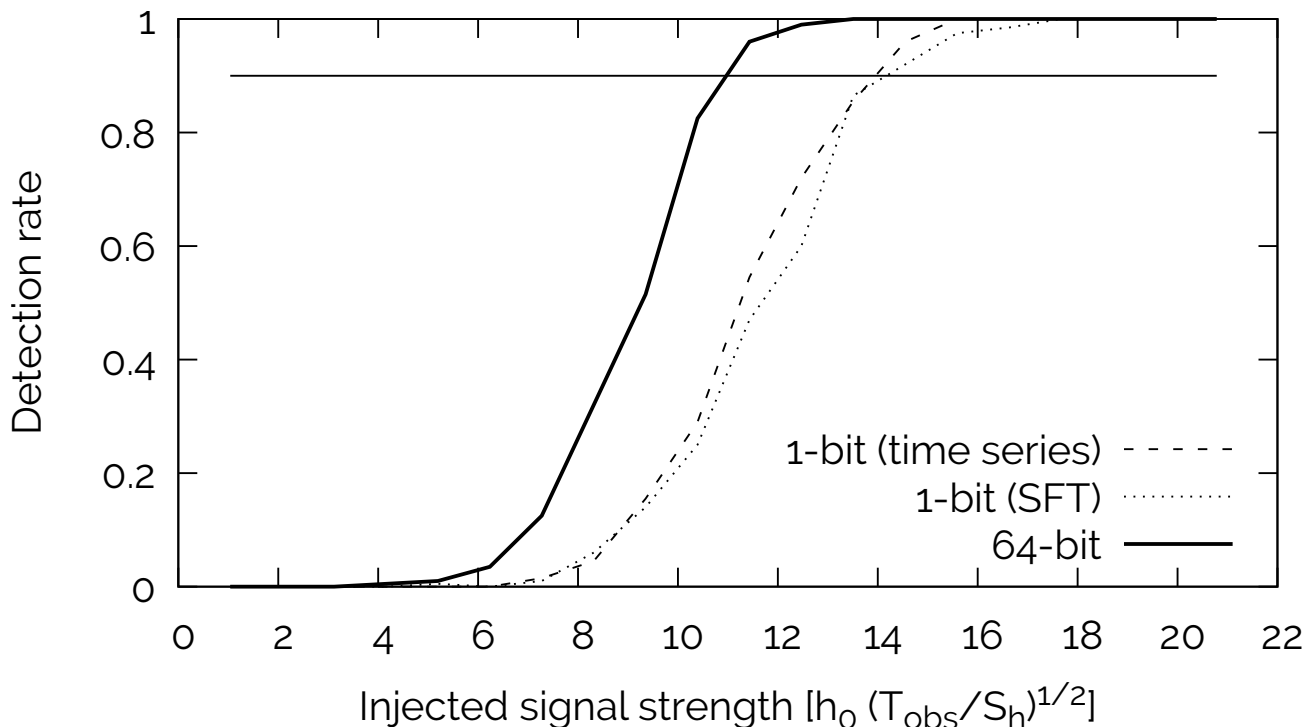


Figure 3. \mathcal{F} -statistic detection fraction versus injected signal-to-noise ratio $h_0 [T_{\text{obs}}/S_h(f_0)]^{1/2}$ for 64-bit time series (control), one-bit time series, and one-bit SFTs (see legend). The detection probability is computed from 200 realisations, with $2\mathcal{F}(f_0) > 40.96$ counting as a detection from equation (7) with $\alpha_N = 0.01$. The horizontal line corresponds to 90 per cent detection probability.

the noise-only case, with time series digitisation, which is predicted theoretically to be $\chi_4^2(\lambda = 0; 2\mathcal{F})$ (solid curve). The top right panel shows the \mathcal{F} -statistic PDF when a signal is present, again with digitisation in the time series, which is predicted to be $\chi_4^2(\lambda \neq 0; 2\mathcal{F})$ (solid curve). The empirical PDFs (dashed curves) are generated from 10^5 realisations of the \mathcal{F} -statistic by selecting $2\mathcal{F}$ from a frequency bin where the signal is absent (top left panel) and present (top right and bottom panels).

The cause of the distortion in the PDF of the \mathcal{F} -statistic, when digitising the SFT, is uncertain. Empirically, when only noise is present, multiplying $2\mathcal{F}$ by a scale factor $s = 1.47$ restores the PDF to the expected shape, that is, $2s\mathcal{F}$ (rather than $2\mathcal{F}$) is χ_4^2 distributed. The value of s is not affected by the choice of T_{obs} , the length of time covered by each SFT, or the right ascension or declination searched. When processing the data at progressively higher precision,

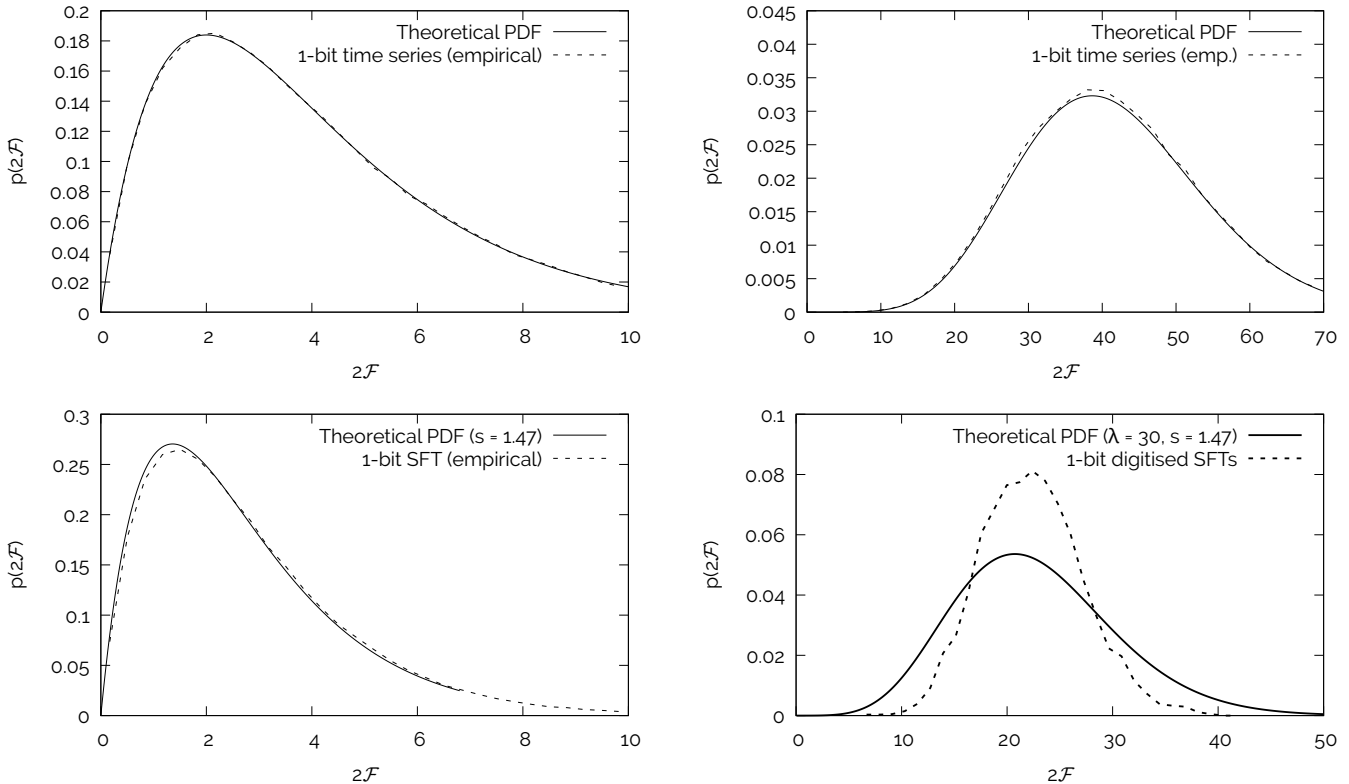


Figure 4. Probability density function (PDF) for the \mathcal{F} -statistic operating on one-bit digitised data. The left column shows noise-only realisations, while the right column shows noise plus an injected signal. The top row shows digitisation of the time series, and the bottom row shows digitisation of the SFTs. In all panels, the dotted curve is the empirical PDF derived from Monte Carlo simulations with 10^5 realisations. For the top row, the solid curve shows the theoretically expected PDFs for 64-bit digitisation, namely a chi-squared distribution (top left) and a non-central chi-squared distribution (non-centrality parameter $\lambda = 37$). The empirical distributions for the time-series digitised data are good fits to the theory, as discussed in Section 4.3. By contrast, the empirical PDFs in the bottom row (where the SFTs are digitised) are distorted significantly compared to the PDF for 64-bit digitisation. In the noise-only case (bottom left panel), an *ad hoc* scaling factor $s = 1.47$ produces a good match (see Section 4.3). However, no simple scaling can reproduce a chi-squared distribution when digitising data containing an injected signal (bottom right panel; non-centrality parameter $\lambda = 30$ chosen as best fit with scale factor $s = 1.47$).

the PDF converges on the chi-squared distribution, becoming indistinguishable by eye at about five-bit precision, when using the output levels recommended by Max (1960).

In the bottom-right panel of Figure 4 we plot the PDF of the \mathcal{F} -statistic in the noise plus signal case, operating on one-bit digitised SFTs, with the object of testing whether $2\mathcal{F}$ follows a non-central chi-squared distribution in the presence of a signal. The PDF is determined through Monte Carlo simulations containing a strong injection, $h_0 = 2 \times 10^{-24}$, with other parameters given in Table 1. Adopting the scaling factor $s = 1.47$ from the noise case, we fit a non-central chi-squared distribution with four degrees of freedom. This fit finds the best-fit non-centrality parameter $\lambda = 29.5$, but the resulting curve is a poor fit to the empirical PDF, which is narrower and more sharply-peaked. This implies that the PDF distortion occurs for both noise and signal (i.e. it is not restricted to one or the other), and that the scale factor s does not work for a signal even though it works for noise. These tests may help inform future work to identify the cause of the distortion.

4.4. Frequency evolution

Isolated neutron stars spin down due to electromagnetic braking (Melatos 1997). The performance of a coherent matched filter like the \mathcal{F} -statistic degrades, if the source frequency evolves significantly over the observation period, unless the frequency evolution is known and accounted for when computing the \mathcal{F} -statistic. As the frequency evolution of the source is often not known precisely (for example, because of uncertainties in electromagnetic measurements of

spin frequency, or because the frequency evolution incorporates stochastic terms), it is important to compare the loss of sensitivity caused by a changing source frequency between the 64-bit and fewer-bit cases.

For the purposes of this paper, we model the spin down by the leading term in the Taylor expansion proportional to $\dot{f} \neq 0$ in the `lalpulsar_Makefakedata_v4` signal phase while taking $\dot{f} = 0$ in the \mathcal{F} -statistic². (Jaranowski et al. 1998) We compare the percentage sensitivity loss with one-, two- and 64-bit digitisation and two-bit digitisation (using optimal thresholds) for $0 \leq \dot{f} \leq 2 \times 10^{-11} \text{ Hz s}^{-1}$. For $\dot{f} > 2 \times 10^{-11} \text{ Hz s}^{-1}$ (with the parameters selected in Table 1), the signal cannot be detected reliably even with 64 bits. The results are displayed in Figure 5. The few-bit curves are parallel to the 64-bit curve for all \dot{f} , implying that few-bit digitisation does not produce any *extra* loss of sensitivity due to $\dot{f} \neq 0$, over and above the loss of sensitivity measured in Section 4.2.

5. REALISTIC NOISE

The tests in Section 4 assume white, Gaussian noise. In this section, we examine those two assumptions and use data collected by LIGO as background noise to test how digitisation performs, when these assumptions are weakened.

Although the noise power spectrum of the LIGO detectors varies substantially over its operating band (Aasi et al. 2015a), continuous-wave searches based on the \mathcal{F} -statistic are typically broken up into multiple subsearches addressing narrow subbands (typically 1 Hz wide) covering only a small part of the total operating band. Therefore, we can safely take the noise spectrum in each subband to be approximately flat (i.e. white noise). The same is true when digitising the time series, as long as the data are bandpass filtered (otherwise the digitisation tends to track sinusoidal variation of large noise lines).

While Gaussian noise is often assumed for the purpose of benchmarking different detection strategies (Jaranowski et al. 1998), in practice LIGO detector noise is routinely non-Gaussian, and varies depending on the detector, observation start time, and frequency band (Aasi et al. 2015c). It is beyond the scope of this paper to exhaustively analyse LIGO detector noise; for an example of recent discussion of data quality in Advanced LIGO see Covas et al. (2018).

Nonetheless, it is instructive to perform some representative investigations of whether digitisation remains effective with non-white and non-Gaussian noise. We repeat the tests from Section 4 in two ways: we attempt to detect hardware injections made during LIGO’s sixth science run (S6), and we attempt to detect synthetic signals injected on top of S6 data in software. In the latter case, we investigate the effect of varying the sky position, search frequency band, and observation start time.

5.1. S6 hardware injections

LIGO’s Science Run 6 (S6) ran from July 2009 to October 2010. During that observing run, the LIGO Observatory injected signals for ten mock pulsars into the data stream by direct excitation of the interferometer mirrors (Abadie et al. 2012).

We search for each hardware injection in the raw 64-bit data, from both initial LIGO detectors (Hanford and Livingston). We then repeat the search using two different digitisation strategies: a one-bit time series, representing the most extreme case, and a two-bit time series, digitised using the optimal thresholds described above. When digitising, we first apply a bandpass filter that admits only a 2 Hz frequency band around the injection. Because some pulsars have significant spin-down, we explicitly include the injected value of \dot{f} when using `lalpulsar_ComputeFstatistic_v2` to calculate the \mathcal{F} -statistic. Otherwise, the search is performed as described in Section 4.1.

The \mathcal{F} -statistic values for the one-, two- and 64-bit searches are presented for comparison in Table 3. The injected pulsars vary widely in h_0 , so we do not detect all of them, even in 64-bit data. For reference, the table also gives the \mathcal{F} -statistic values predicted by the LALSuite routine `lalpulsar_PredictFstat`, which gives an estimate for $2\mathcal{F}$ based on the observed detector noise and the parameters of the injected signal over the designated observing time. The predictions give a sense of whether the signal should be detectable, and also serve as a check that values of $2\mathcal{F}$ returned by the double-precision search are sensible. The results are broadly consistent with Section 4.2, in the sense that two-bit digitisation reduces $2\mathcal{F}$, for detected pulsars, by about 10–20 per cent (20–30 per cent in one-bit digitisation), although pulsar 4 sees a 50 per cent reduction in $2\mathcal{F}$, which occurs in both digitisation modes tested. In pulsar 3, when digitising, the peak \mathcal{F} -statistic appears 80 bins below where it is expected, corresponding to a reduction in frequency of $5.5 \times 10^{-4} \text{ Hz}$ (the peak appears in the expected bin when processing 64-bit data).

² In practice, `lalpulsar_ComputeFstatistic_v2` can search over \dot{f} , \ddot{f} and $\ddot{\dot{f}}$ but the problem then transfers to higher derivatives, which degrade the sensitivity in an analogous fashion.

Table 3. One-, two- and 64-bit \mathcal{F} -statistic search results for the LIGO Science Run 6 hardware injections, using a 20-hr stretch of data starting at GPS time 946 475 008 s. The pulsar indices and injection frequencies f_0 are those given in Abbott et al. (2007). The injections have $\dot{f} \neq 0$, which is treated as a known parameter and accounted for directly in `lalpulsar_ComputeFstatistic_v2`. Column four gives the value of $2\mathcal{F}$ predicted by the LALSuite code `lalpulsar_PredictFstat`. The detection threshold is $2\mathcal{F}_c = 3.9 \times 10^1$ for false alarm probability $\alpha = 0.01$ over the 1 Hz search band. For the injections that are detected, marked by *, we report the reduction in $2\mathcal{F}$ when digitising the time series to two-bits using optimal thresholds (columns six and seven), and to one-bit (columns eight and nine). In pulsar 3, marked by †, the peak in $2\mathcal{F}$ we report for digitised data is shifted by 5.5×10^{-4} Hz from the frequency bin expected to contain the signal.

Index	f_0 (Hz)	h_0	Predicted $2\mathcal{F}$	$2\mathcal{F}$ (64-bit)	$2\mathcal{F}$ (two-bit)	$2\mathcal{F}_{1 \text{ bit}}/2\mathcal{F}_{64 \text{ bit}}$	$2\mathcal{F}$ (one-bit)	$2\mathcal{F}_{1 \text{ bit}}/2\mathcal{F}_{64 \text{ bit}}$
0	265.5	2.47×10^{-25}	4.7	8.5	4.6	–	13	–
1	849.1	1.06×10^{-24}	4.8	16	10	–	0.18	–
2*	575.2	4.02×10^{-24}	99	80	68	0.85	61	0.76
3*	108.9	1.63×10^{-23}	430	304	261†	0.86	231†	0.76
4*	1430	4.56×10^{-23}	560	539	287	0.53	250	0.46
5	52.8	4.85×10^{-24}	4.9	4.1	5.7	–	2.7	–
6	148.7	6.92×10^{-25}	4.9	1.1	2.3	–	7.5	–
7	1221	2.20×10^{-24}	9.3	0.48	5.0	–	4.5	–
8*	194.3	1.59×10^{-23}	440	499	424	0.85	346	0.70
9	763.8	8.13×10^{-25}	4.7	8.6	6.3	–	8.4	–

5.2. Software injections

Ten hardware injections are too few from which to infer reliably a detection threshold corrected for non-Gaussian noise. To estimate the sensitivity loss when digitising actual, non-Gaussian data, we take a segment of detector output from S6 and inject synthetic signals into it. The synthetic signals are generated in the frequency domain by `lalpulsar_Makefakedata_v4`, which can use the S6 detector SFTs in lieu of Gaussian noise. We digitise the time series by computing the inverse Fourier transform, digitising it, then computing the forward Fourier transform. The SFTs cover the 1 Hz search band, so the above procedure effectively bandpass filters the data. When digitising in two bits, we use the optimal thresholds. The search procedure and detection criterion are otherwise the same as described in Section 4.1. We then compare the signal strengths needed for detection in one-, two- and 64-bit data. For the one-bit case, we test digitising in both the time series and the SFTs.

In order to perform a large number of Monte-Carlo-style trials, we exploit the natural variation in the data in three ways: varying right ascension α , varying f_0 , and using different stretches of S6 data. We compare 64-bit against digitised data by taking a signal at the threshold of detectability, when in 64-bit data, and measuring how much stronger that signal needs to be, in order to be detectable in digitised data. We quantify this using $B = h_{0,\text{min,digitised}}/h_{0,\text{min,64 bit}}$, where $h_{0,\text{min}}$ is the lowest-strength signal that can be detected (i.e. the lowest h_0 with $2\mathcal{F} > 2\mathcal{F}_c$).

When varying α , we use a single 10-hr stretch of data (from both detectors) and try 189 choices of right ascension α uniformly separated by 0.005 rad between $\alpha = 0.01$ rad and $\alpha = 0.95$ rad. Other parameters are given in Table 1. The value of B for each trial is shown in Figure 6, and the average B for those trials is given in Table 4. In this case, one-bit time-series digitisation is actually an improvement over the results in Section 4.2: with real data, we find $B \approx 1.1$ (compared to $B \approx 1.3$ in our trials with Gaussian noise). In contrast, the results for SFT digitisation are worse, returning $B = 1.95$ (compared to $B = 1.29$ in trials with Gaussian noise). The two-bit case improves over the one-bit (time series) case by around eight per cent.

When varying f_0 , we use a single 10-hr stretch of data and inject signals at $0.2 \text{ kHz} \leq f_0 \leq 1 \text{ kHz}$. The injection frequency f_0 is selected by drawing randomly from a uniform distribution over that range, and other parameters are given in Table 1. The loss in sensitivity for the one-bit digitised time series is close to what we observe in Section 4.2: for realistic data, we find $B \approx 1.2$, compared to $B \approx 1.3$ for trials on Gaussian noise. Digitising the time series to two-bits produces only a slight improvement, of around two per cent. The SFT digitised data performs better in this trial than when varying α , with $B \approx 1.4$, although it is still worse than the Gaussian noise trials (which show $B \approx 1.3$). We do not observe a frequency dependence in B .

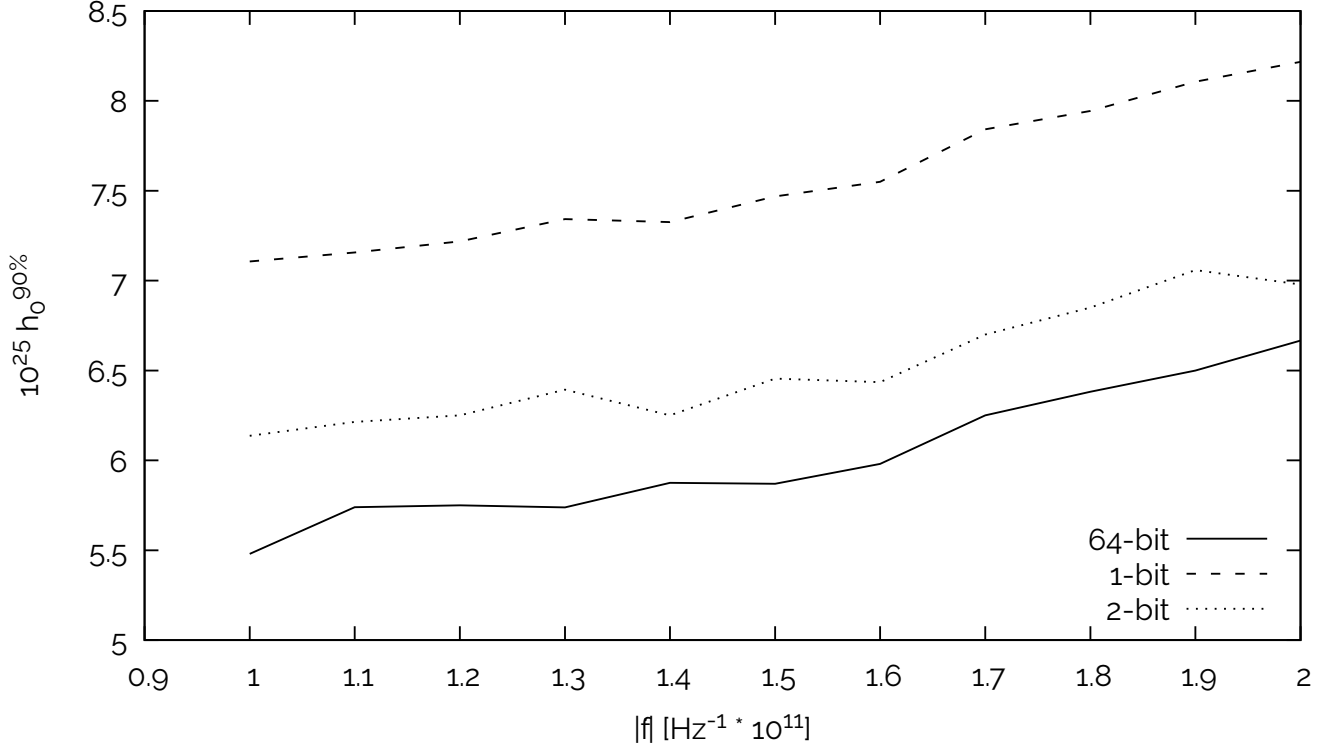


Figure 5. Sensitivity loss caused by digitisation versus spin-down rate \dot{f} (horizontal axis; units 10^{11}Hz^{-1}). The vertical axis gives the wave strain $h_0^{90\%}$ of the injected signal necessary for a 90 per cent probability of detection. As expected, as $|\dot{f}|$ increases, so does $h_0^{90\%}$, but the slope of the $h_0^{90\%}$ versus $|\dot{f}|$ curve is roughly the same for one-bit (dashed line), two-bit (dotted line) and 64-bit (solid line) digitisation.

Table 4. Mean of sensitivity loss factor $B = h_{0,\text{min,digitised}}/h_{0,\text{min,64 bit}}$, measuring how much stronger a signal must be to be detected in one-bit and two-bit digitised data versus 64-bit digitised data, for a signal injected into realistic background noise from LIGO Science Run 6. Two-bit digitisation is performed using the optimal thresholds. We vary sky position, source frequency, and observation starting time to produce multiple realisations.

Test	Realisations	B (2-bit time series)	B (1-bit time series)	B (1-bit SFT)
Sky positions	189	1.10	1.19	1.95
Frequencies	200	1.28	1.31	2.61
Start times	50	1.26	1.32	1.99

When varying the start time, we identify 50 non-overlapping ten-hour segments of S6 data. While not every such segment is complete, all selected segments have a duty cycle over 89 per cent, and the \mathcal{F} -statistic can be calculated even in the presence of data gaps. We inject a signal, whose parameters are given in Table 1, into each segment and search for it in digitised and undigitised data. The results are similar to those for Gaussian noise for both one- and two-bit digitisation of the time series. The performance of SFTs is worse, with $B \approx 1.99$; that is, a signal needs to be roughly twice as strong to be detectable.

Overall, the results in Table 4 are promising: they show that digitising the time series to one bit yields $1.19 \lesssim B \lesssim 1.32$ (two bits $1.10 \lesssim B \lesssim 1.26$) for a range of different trials with realistic noise. Digitising the SFTs yields $1.4 \lesssim B \lesssim 2.5$. The results suggest that digitisation of the time series works roughly as well on real data as on synthetic data, even without post-processing the data to make it more amenable to digitisation (other than bandpass filtering to the search band) through procedures such as whitening (Cuoco et al. 2001); these procedures may be necessary

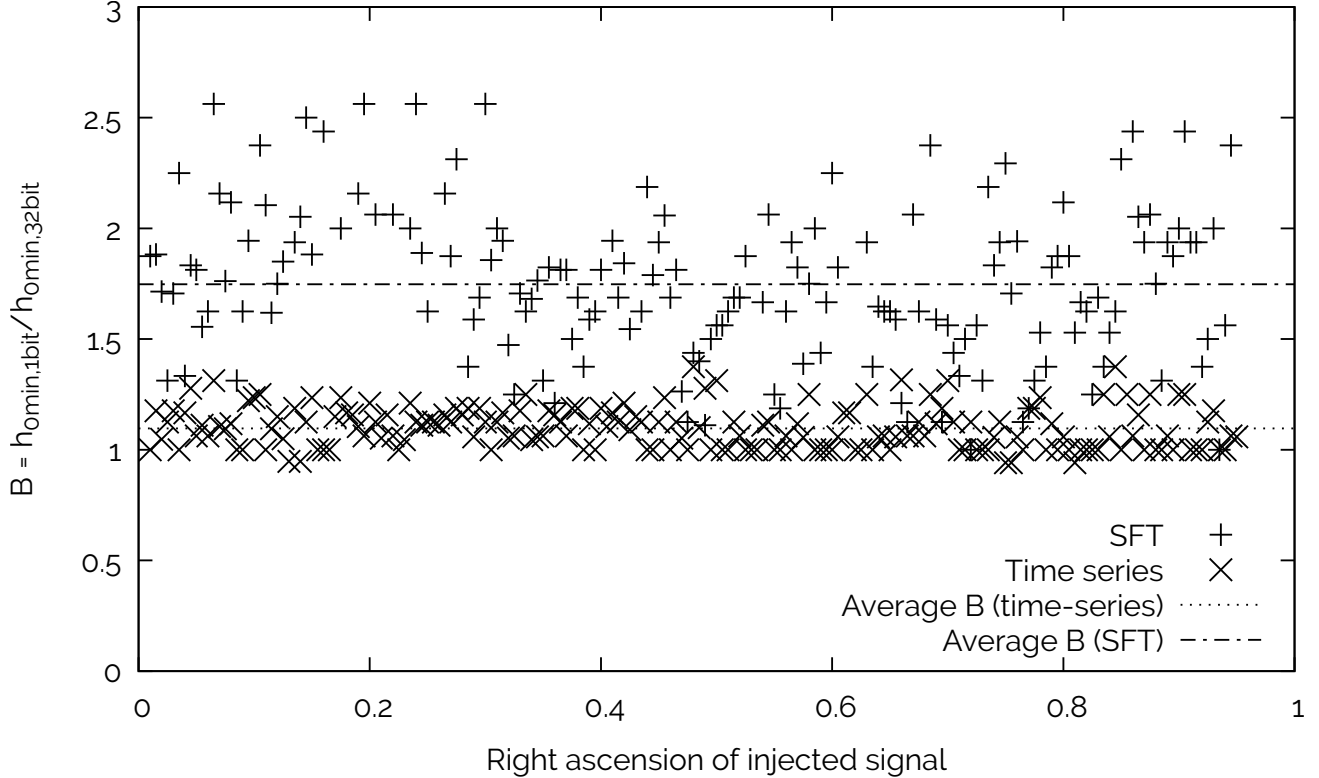


Figure 6. Sensitivity loss factor $B = h_{0,\min,1\text{ bit}}/h_{0,\min,64\text{ bit}}$ for one-bit digitisation of both the time series and SFT, showing 189 realisations with different α (horizontal axis). The crosses show B for one-bit digitised time series, and the pluses show B for 1-bit digitised SFTs. The average B is shown by the dotted (one-bit time series digitisation) and dot-dashed (one-bit SFT digitisation) lines, which are the numbers reported in Table 4.

when digitising the SFTs. This is consistent with the result of the analytic calculation in the Appendix, namely that the autocorrelation function of a one-bit digitised signal is independent of the power-law exponent for a fat-tailed noise PDF and depends weakly on the parameters of a thin-tailed noise PDF, e.g. modelled as an admixture of two Gaussians.

6. CONCLUSION

This paper shows that, when digitising 64-bit interferometer strain data down to one or two bits, \mathcal{F} -statistic-based gravitational wave searches remain viable, with a modest sensitivity penalty. This translates to a factor of 64 or 32 saving in memory, for a sensitivity penalty of around 25 per cent (one-bit digitisation) or 6.4 per cent (two-bit digitisation).

In any application of digitisation, careful thought should be put into designing the data pipeline so that digitisation is performed at the most effective place. For systems that are storage-limited, this might be how the data are stored before processing. For systems that are bandwidth limited, data might be digitised before transfer. For systems that are memory-limited, digitisation may be performed as the data are streamed from storage into memory. We emphasise that continuous wave searches are not memory-limited normally at the time of writing, so the case for sacrificing sensitivity to save memory is marginal, even though the sensitivity loss is modest. However, it is hard to predict the future of gravitational wave astronomy reliably at such an early juncture. Future advances in search algorithms, data collection practices, data volumes, and interferometer designs may create a need for memory savings, just as occurred historically with the move to baseband recording in pulsar radio astronomy, e.g. [Stairs et al. \(2000\)](#). If a need for memory savings does emerge in the future, the results in this paper provide some preliminary comfort, that digitisation can help, and that the impact on sensitivity is tolerable.

Places where few-bit digitisation is worth exploring include I/O-constrained environments, for example cloud-based searches on commodity commercial providers (such as Amazon Web Services), or massively distributed volunteer

computing projects such as Einstein@Home (Knispel et al. 2010; Abbott et al. 2017a) through the Berkeley Open Infrastructure for Network Computing (BOINC) project. Digitisation may also be helpful in novel computing environments that might be developed in the future, where computing power is plentiful but memory or transfer is constrained. A prototypical example of this evolution is graphics processing units: while they now have adequate memory bandwidth for the searches described in this paper, early GPUs had directional, high-latency transfer busses and a low ratio of I/O to compute resources. Digitisation to four- or eight-bits also results in negligible sensitivity loss while delivering memory savings and should be considered.

While no changes are necessary to the algorithms in `lalpulsar.ComputeFstatistic.v2` for \mathcal{F} -statistic-based searches, a new storage format for time series or SFT files needs to be developed. This could be integrated into the LIGO Algorithms Library, or could be a stand-alone wrapper, which converts from the compact digitised form to the standard format in RAM. Continuous wave search algorithms that use reduced precision modular arithmetic on a complex lattice have also been developed previously (Dergachev 2016).

APPENDIX

A. ONE-BIT DIGITISATION OF NON-GAUSSIAN NOISE

In this appendix, we investigate theoretically the effect of digitisation on non-Gaussian noise, by considering a simplified analogy of the detection process following the approach in Vleck & Middleton (1966). Specifically, we analyse the temporal autocorrelation function of a noisy data stream as a loose proxy for a matched filter such as the \mathcal{F} -statistic, noting that the matched filter itself is too challenging to study directly in the analytic fashion introduced by Vleck & Middleton (1966). We emphasise that the results in the appendix are illustrative and pedagogical; they should not be applied to interpret quantitatively the empirical results in Sections 4 and 5. For simplicity, we consider one-bit digitisation implemented according to Equation (8). For definiteness, we consider a noise process, whose PDF is either fat-tailed (power-law) or thin-tailed (sum of two Gaussians). The analysis can be generalised directly to multiple bits and PDF tails with other functional forms with minimal alterations.

Consider a noisy time series $x(t)$. Define the random variables $X = x(t)$ and $Y = x(t + \tau)$. The correlation function $r(\tau) = \langle x(t)x(t + \tau) \rangle$ is given by the covariance of X and Y , namely

$$r(\tau) = \langle XY \rangle \tag{A1}$$

$$= \int_{-\infty}^{\infty} dX \int_{-\infty}^{\infty} dY XY p(X, Y), \tag{A2}$$

where $p(X, Y)$ is the joint PDF, i.e., $p(X, Y)dX dY$ equals the probability of measuring $X \leq x(t) \leq X + dX$ and $Y \leq x(t + \tau) \leq Y + dY$.

Now suppose that the noisy time series is digitised to one bit to give the time series $\tilde{x}(t) = f[x(t)]$, with

$$f(X) = \begin{cases} 1 & \text{for } X \geq 0 \\ -1 & \text{for } X < 0. \end{cases} \tag{A3}$$

By the argument leading to equation (A1), the covariance of the one-bit digitised signal is given by

$$R(\tau) = \int_{-\infty}^{\infty} dX \int_{-\infty}^{\infty} dY f(X)f(Y)p(X, Y). \tag{A4}$$

We now ask: what is $R(\tau)$ in terms of $r(\tau)$? Specifically, what is $R(\tau)/r(\tau)$ in the low-signal-to-noise regime $r(\tau) \ll 1$ applicable to gravitational wave searches? Strictly speaking, the relevant figure of merit for gravitational wave searches is actually the ratio of the specific detection statistic (e.g, the \mathcal{F} -statistic in this paper) for one- and 64-bit digitisation, but the latter calculation lies beyond the scope of this paper, as noted above. Instead, we use the correlation function ratio $R(\tau)/r(\tau)$ as a loose analogy for the \mathcal{F} -statistic ratio. There is no guarantee that the ratio $R(\tau)/r(\tau)$ behaves the same way as the \mathcal{F} -statistic ratio. The goal is merely to check for broad, qualitative consistency with the empirical findings in Sections 4 and 5, e.g. that the sensitivity loss does not depend on search parameters in either Gaussian or non-Gaussian noise, within an analytic framework.

Following [Vleck & Middleton \(1966\)](#), we separate the integral (A4) with (A3) into four quadrants to obtain:

$$\begin{aligned} R(\tau) &= \int_0^\infty dX \int_0^\infty dY p(X, Y) - \int_0^\infty dX \int_{-\infty}^0 dY p(X, Y) \\ &\quad - \int_{-\infty}^0 dX \int_0^\infty dY p(X, Y) + \int_{-\infty}^0 dX \int_{-\infty}^0 dY p(X, Y) \end{aligned} \quad (\text{A5})$$

$$= -1 + 4 \int_0^\infty dX \int_0^\infty dY p(X, Y), \quad (\text{A6})$$

where (A6) follows from (A5) by using the normalisation condition $1 = \int_{-\infty}^\infty dX \int_{-\infty}^\infty dY p(X, Y)$. [Vleck & Middleton \(1966\)](#) evaluated (A6) for the two-dimensional Gaussian PDF

$$p(X, Y) = (2\pi)^{-1} |\det \Sigma|^{-1/2} \exp(-\mathbf{x} \Sigma^{-1} \mathbf{x}^T / 2), \quad (\text{A7})$$

with

$$\mathbf{x} = (X \ Y), \quad (\text{A8})$$

$$\Sigma = \begin{pmatrix} \sigma^2 & r \\ r & \sigma^2 \end{pmatrix}, \quad (\text{A9})$$

where $\sigma^2 = \langle X^2 \rangle = \langle Y^2 \rangle$ is the variance, and $r = \langle XY \rangle$ is the covariance. The result is

$$R(\tau) = \frac{2}{\pi} \sin^{-1} \left[\frac{r(\tau)}{\sigma^2} \right]. \quad (\text{A10})$$

In [Section 5](#) and this appendix, we are interested in how equation (A10) generalises for non-Gaussian noise. Non-Gaussianity takes several forms. One useful limit is a fat-tailed PDF, e.g. a PDF with a power-law tail, where large noise spikes are more common than a Gaussian process would predict. This situation occurs whenever the interferometer is prone to “glitches” or experiences elevated levels of seismic noise ([Aasi et al. 2015c](#)). Another useful limit is a thin-tailed PDF, where large noise spikes are less common than a Gaussian process would predict. This can happen when, for example, the interferometer noise is bistable, switching randomly between a low and high state, so that the PDF is the sum of a narrow and broad Gaussian. We consider both limits briefly below.

Consider, for the sake of definiteness, a family of fat-tailed PDFs given by the two-dimensional Student’s t -distribution

$$p(X, Y) = (2\pi)^{-1} |\det \Sigma|^{-1/2} (1 + \nu^{-1} \mathbf{x} \Sigma^{-1} \mathbf{x}^T)^{-(2+\nu)/2} \quad (\text{A11})$$

with

$$\Sigma = \frac{\nu - 2}{\nu} \begin{pmatrix} \sigma^2 & r \\ r & \sigma^2 \end{pmatrix} \quad (\text{A12})$$

instead of (A9). Again the covariance satisfies $\langle XY \rangle = r$ and the variance satisfies $\langle X^2 \rangle = \langle Y^2 \rangle = \sigma^2$. The covariance is meaningful only for $\nu > 2$. Note that we do *not* claim that LIGO detector noise obeys the PDF (A11), although it is a fair approximation at certain epochs, when the interferometer “glitches”. Rather, equation (A11) offers a convenient way to parameterise fat-tailed, non-Gaussian noise.

Upon substituting (A11) and (A12) into (A6), we obtain the result

$$R(\tau) = \frac{2}{\pi} \sin^{-1} \left[\frac{r(\tau)}{\sigma^2} \right]. \quad (\text{A13})$$

Remarkably, equation (A13) is identical to equation (A10) for all values of ν , i.e., for all values of the exponent of the power-law tail. The reduction in the covariance is the same for Gaussian and non-Gaussian noise modelled by the PDFs (A7) and (A11). A qualitatively similar result can be proved for any PDF which is a function of $\mathbf{x} \Sigma^{-1} \mathbf{x}^T$ by rotating coordinates in (A6) to the principal axes of the ellipse $\mathbf{x} \Sigma^{-1} \mathbf{x}^T = \text{constant}$.

Now consider a family of thin-tailed PDFs of the form

$$p(X, Y) = \zeta p_1(X, Y) + (1 - \zeta) p_2(XY) \quad (\text{A14})$$

with

$$p_i(X, Y) = (2\pi)^{-1} |\det \Sigma_i|^{-1/2} \exp(-\mathbf{x} \Sigma_i^{-1} \mathbf{x}^T / 2), \quad (\text{A15})$$

$$\mathbf{x} = (X \ Y), \quad (\text{A16})$$

$$\Sigma_i = \begin{pmatrix} \sigma_i^2 & r_i \\ r_i & \sigma_i^2 \end{pmatrix}. \quad (\text{A17})$$

It is straight-forward to confirm that equation (A14) is thin-tailed for $\sigma_1 < \sigma_2$. Upon substituting equation (A14) into equation (A6), we obtain

$$R(\tau) = \frac{2}{\pi} \left\{ \zeta \sin^{-1} \left[\frac{r_1(\tau)}{\sigma_1^2} \right] + (1 - \zeta) \sin^{-1} \left[\frac{r_2(\tau)}{\sigma_2^2} \right] \right\}. \quad (\text{A18})$$

REFERENCES

- Aasi, J., The LIGO Scientific Collaboration, Abbott, B. P., et al. 2015a, *Classical and Quantum Gravity*, 32, 074001, doi: [10.1088/0264-9381/32/7/074001](https://doi.org/10.1088/0264-9381/32/7/074001)
- Aasi, J., Abbott, B. P., Abbott, R., et al. 2015b, *Physical Review D*, 91, 062008, doi: [10.1103/PhysRevD.91.062008](https://doi.org/10.1103/PhysRevD.91.062008)
- Aasi, J., Abadie, J., Abbott, B. P., et al. 2015c, *Classical and Quantum Gravity*, 32, 115012, doi: [10.1088/0264-9381/32/11/115012](https://doi.org/10.1088/0264-9381/32/11/115012)
- Abadie, J., Abbott, B. P., Abbott, R., et al. 2012, *Physical Review D*, 85, 022001, doi: [10.1103/PhysRevD.85.022001](https://doi.org/10.1103/PhysRevD.85.022001)
- Abbott, B., Abbott, R., Adhikari, R., et al. 2005a, *Physical Review D*, 72, 102004, doi: [10.1103/PhysRevD.72.102004](https://doi.org/10.1103/PhysRevD.72.102004)
- . 2005b, *Physical Review Letters*, 94, 181103, doi: [10.1103/PhysRevLett.94.181103](https://doi.org/10.1103/PhysRevLett.94.181103)
- . 2007, *Physical Review D*, 76, 042001, doi: [10.1103/PhysRevD.76.042001](https://doi.org/10.1103/PhysRevD.76.042001)
- Abbott, B. P., Abbott, R., Abbott, T. D., et al. 2017a, *Physical Review D*, 96, 122004, doi: [10.1103/PhysRevD.96.122004](https://doi.org/10.1103/PhysRevD.96.122004)
- . 2017b, *Physical Review D*, 95, 122003, doi: [10.1103/PhysRevD.95.122003](https://doi.org/10.1103/PhysRevD.95.122003)
- . 2019, *Physical Review D*, 100, 122002, doi: [10.1103/PhysRevD.100.122002](https://doi.org/10.1103/PhysRevD.100.122002)
- Abbott, R., Abbott, T. D., Acernese, F., et al. 2022a, *Physical Review D*, 105, 022002, doi: [10.1103/PhysRevD.105.022002](https://doi.org/10.1103/PhysRevD.105.022002)
- Abbott, R., Abe, H., Acernese, F., et al. 2022b, *Physical Review D*, 106, 062002, doi: [10.1103/PhysRevD.106.062002](https://doi.org/10.1103/PhysRevD.106.062002)
- Acernese, F., Agathos, M., Agatsuma, K., et al. 2015, *Classical and Quantum Gravity*, 32, 024001, doi: [10.1088/0264-9381/32/2/024001](https://doi.org/10.1088/0264-9381/32/2/024001)
- Akutsu, T., Ando, M., Arai, K., et al. 2021, *Progress of Theoretical and Experimental Physics*, 2021, 05A101, doi: [10.1093/ptep/ptaa125](https://doi.org/10.1093/ptep/ptaa125)
- Allen, B., & Brady, P. 1997, LIGO Technical Note, LIGO-T970128
- Allen, B., Goetz, E., Keitel, D., et al. 2022, LIGO Report T040164-v2
- Astone, P., Colla, A., D'Antonio, S., Frasca, S., & Palomba, C. 2014, *Physical Review D*, 90, 042002, doi: [10.1103/PhysRevD.90.042002](https://doi.org/10.1103/PhysRevD.90.042002)
- Beniwal, D., Clearwater, P., Dunn, L., Melatos, A., & Ottaway, D. 2021, *Physical Review D*, 103, 083009, doi: [10.1103/PhysRevD.103.083009](https://doi.org/10.1103/PhysRevD.103.083009)
- Blackburn, K., Mours, B., Anderson, S., et al. 2009, LIGO Technical Note, LIGO-T970130
- Bondarescu, R., Teukolsky, S. A., & Wasserman, I. 2009, *Physical Review D*, 79, 104003, doi: [10.1103/PhysRevD.79.104003](https://doi.org/10.1103/PhysRevD.79.104003)
- Brady, P. R., & Creighton, T. 2000, *Physical Review D*, 61, 082001, doi: [10.1103/PhysRevD.61.082001](https://doi.org/10.1103/PhysRevD.61.082001)
- Chung, C. T. Y., Melatos, A., Krishnan, B., & Whelan, J. T. 2011, *Monthly Notices of the Royal Astronomical Society*, 414, 2650, doi: [10.1111/j.1365-2966.2011.18585.x](https://doi.org/10.1111/j.1365-2966.2011.18585.x)
- Covas, P. B., Effler, A., Goetz, E., et al. 2018, *Physical Review D*, 97, 082002, doi: [10.1103/PhysRevD.97.082002](https://doi.org/10.1103/PhysRevD.97.082002)
- Cuoco, E., Losurdo, G., Calamai, G., et al. 2001, *Phys. Rev. D*, 64, 122002, doi: [10.1103/PhysRevD.64.122002](https://doi.org/10.1103/PhysRevD.64.122002)
- Dergachev, V. 2012, *Physical Review D*, 85, 062003, doi: [10.1103/PhysRevD.85.062003](https://doi.org/10.1103/PhysRevD.85.062003)
- . 2013, *PhRvD*, 87, 062001, doi: [10.1103/PhysRevD.87.062001](https://doi.org/10.1103/PhysRevD.87.062001)
- . 2016, personal communication
- Dhurandhar, S., Krishnan, B., Mukhopadhyay, H., & Whelan, J. T. 2008, *Physical Review D*, 77, 082001, doi: [10.1103/PhysRevD.77.082001](https://doi.org/10.1103/PhysRevD.77.082001)
- Frigo, M., & Johnson, S. G. 2005, *Proceedings of the IEEE*, 93, 216

- Goetz, E., & Riles, K. 2011, *Classical and Quantum Gravity*, 28, 215006,
doi: [10.1088/0264-9381/28/21/215006](https://doi.org/10.1088/0264-9381/28/21/215006)
- Idrisy, A., Owen, B. J., & Jones, D. I. 2015, *Physical Review D*, 91, 024001, doi: [10.1103/PhysRevD.91.024001](https://doi.org/10.1103/PhysRevD.91.024001)
- IEEE. 2008, *IEEE Std 754-2008*,
doi: [10.1109/IEEESTD.2008.4610935](https://doi.org/10.1109/IEEESTD.2008.4610935)
- Jaranowski, P., Królak, A., & Schutz, B. F. 1998, *Physical Review D*, 58, 063001, doi: [10.1103/PhysRevD.58.063001](https://doi.org/10.1103/PhysRevD.58.063001)
- Janet, F. A., & Anderson, S. B. 1998, *Publications of the Astronomical Society of the Pacific*, 110, 1467,
doi: [10.1086/316273](https://doi.org/10.1086/316273)
- Knispel, B., Allen, B., Cordes, J. M., et al. 2010, *Science*, 329, 1305, doi: [10.1126/science.1195253](https://doi.org/10.1126/science.1195253)
- Krishnan, B., Sintes, A. M., Papa, M. A., et al. 2004, *Physical Review D*, 70, 082001,
doi: [10.1103/PhysRevD.70.082001](https://doi.org/10.1103/PhysRevD.70.082001)
- LIGO Scientific Collaboration, Virgo Collaboration, & KAGRA Collaboration. 2018, *LVK Algorithm Library - LALSuite*, Free software (GPL),
doi: [10.7935/GT1W-FZ16](https://doi.org/10.7935/GT1W-FZ16)
- Manchester, R. N., Lyne, A. G., D'Amico, N., et al. 1996, *Monthly Notices of the Royal Astronomical Society*, 279, 1235, doi: [10.1093/mnras/279.4.1235](https://doi.org/10.1093/mnras/279.4.1235)
- Max, J. 1960, *Information Theory*, *IRE Transactions on*, 6, 7, doi: [10.1109/TIT.1960.1057548](https://doi.org/10.1109/TIT.1960.1057548)
- Meadors, G. D., Goetz, E., & Riles, K. 2016, *Classical and Quantum Gravity*, 33, 105017,
doi: [10.1088/0264-9381/33/10/105017](https://doi.org/10.1088/0264-9381/33/10/105017)
- Meadors, G. D., Krishnan, B., Papa, M. A., Whelan, J. T., & Zhang, Y. 2018, *PhRvD*, 97, 044017,
doi: [10.1103/PhysRevD.97.044017](https://doi.org/10.1103/PhysRevD.97.044017)
- Melatos, A. 1997, *Monthly Notices of the Royal Astronomical Society*, 288, 1049,
doi: [10.1093/mnras/288.4.1049](https://doi.org/10.1093/mnras/288.4.1049)
- Melatos, A., Clearwater, P., Suvorova, S., et al. 2021, *Physical Review D*, 104, 042003,
doi: [10.1103/PhysRevD.104.042003](https://doi.org/10.1103/PhysRevD.104.042003)
- Melatos, A., Douglass, J. A., & Simula, T. P. 2015, *Astrophysical Journal*, 807, 132,
doi: [10.1088/0004-637X/807/2/132](https://doi.org/10.1088/0004-637X/807/2/132)
- Melatos, A., & Payne, D. J. B. 2005, *Astrophysical Journal*, 623, 1044, doi: [10.1086/428600](https://doi.org/10.1086/428600)
- Middleton, H., Clearwater, P., Melatos, A., & Dunn, L. 2020, *Physical Review D*, 102, 023006,
doi: [10.1103/PhysRevD.102.023006](https://doi.org/10.1103/PhysRevD.102.023006)
- Millhouse, M., Strang, L., & Melatos, A. 2020, *Physical Review D*, 102, 083025,
doi: [10.1103/PhysRevD.102.083025](https://doi.org/10.1103/PhysRevD.102.083025)
- Pletsch, H. J. 2010, *PhRvD*, 82, 042002,
doi: [10.1103/PhysRevD.82.042002](https://doi.org/10.1103/PhysRevD.82.042002)
- Pletsch, H. J., & Allen, B. 2009, *PhRvL*, 103, 181102,
doi: [10.1103/PhysRevLett.103.181102](https://doi.org/10.1103/PhysRevLett.103.181102)
- Prix, R. 2007, *Physical Review D*, 75, 023004,
doi: [10.1103/PhysRevD.75.023004](https://doi.org/10.1103/PhysRevD.75.023004)
- Prix, R. 2011, *LIGO Report T0900149*
- Sammut, L., Messenger, C., Melatos, A., & Owen, B. J. 2014, *Physical Review D*, 89, 043001,
doi: [10.1103/PhysRevD.89.043001](https://doi.org/10.1103/PhysRevD.89.043001)
- Stairs, I. H., Splaver, E. M., Thorsett, S. E., Nice, D. J., & Taylor, J. H. 2000, *MNRAS*, 314, 459,
doi: [10.1046/j.1365-8711.2000.03306.x](https://doi.org/10.1046/j.1365-8711.2000.03306.x)
- Suvorova, S., Clearwater, P., Melatos, A., et al. 2017, *Physical Review D*, 96, 102006,
doi: [10.1103/PhysRevD.96.102006](https://doi.org/10.1103/PhysRevD.96.102006)
- Suvorova, S., Sun, L., Melatos, A., Moran, W., & Evans, R. J. 2016, *Physical Review D*, 93, 123009,
doi: [10.1103/PhysRevD.93.123009](https://doi.org/10.1103/PhysRevD.93.123009)
- Tenorio, R., Modafferi, L. M., Keitel, D., & Sintes, A. M. 2022, *PhRvD*, 105, 044029,
doi: [10.1103/PhysRevD.105.044029](https://doi.org/10.1103/PhysRevD.105.044029)
- Ushomirsky, G., Cutler, C., & Bildsten, L. 2000, *MNRAS*, 319, 902, doi: [10.1046/j.1365-8711.2000.03938.x](https://doi.org/10.1046/j.1365-8711.2000.03938.x)
- Vleck, J. H. V., & Middleton, D. 1966, *Proceedings of the IEEE*, 54, 2, doi: [10.1109/PROC.1966.4567](https://doi.org/10.1109/PROC.1966.4567)
- Wette, K. 2015, *PhRvD*, 92, 082003,
doi: [10.1103/PhysRevD.92.082003](https://doi.org/10.1103/PhysRevD.92.082003)
- . 2016, *PhRvD*, 94, 122002,
doi: [10.1103/PhysRevD.94.122002](https://doi.org/10.1103/PhysRevD.94.122002)
- Wette, K., Walsh, S., Prix, R., & Papa, M. A. 2018, *Physical Review D*, 97, 123016,
doi: [10.1103/PhysRevD.97.123016](https://doi.org/10.1103/PhysRevD.97.123016)